

CMOS-Compatible Antimony-Doped Germanium Epilayers for Mid-Infrared Low-Loss High-Plasma-Frequency Plasmonics

Haining Chong,[†] Zemin Xu,[†] Zhewei Wang,[†] Jianbo Yu,[†] Tobias Biesner,[‡] Martin Dressel,[‡] Lan Wu,[†] Qiang Li,^{*,†} and Hui Ye^{*,†}

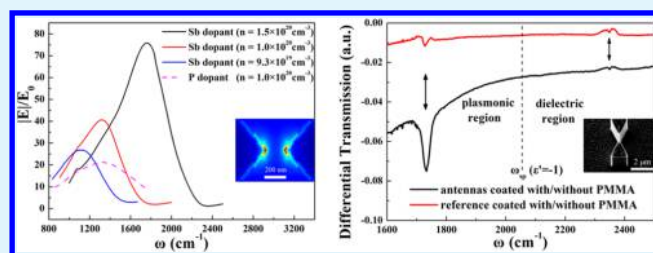
[†]State Key Laboratory of Modern Optical Instrumentation, College of Optical Science and Engineering, Zhejiang University, Hangzhou 310027, China

[‡]Physikalisches Institut, Universität Stuttgart, Pfaffenwaldring 57, 70550 Stuttgart, Germany

Supporting Information

ABSTRACT: Antimony (Sb) heavily-doped germanium (Ge)-on-silicon (Si) epitaxial films are investigated as mid-infrared (MIR) plasmonic materials. Structural, electrical, and optical properties have been improved by proper choice of dopant species (i.e., Sb) and optimization of the growth parameters (i.e., Sb flux and substrate temperature). The increased electron conductivity can be attributed to the elevated carrier concentration ($1.5 \times 10^{20} \text{ cm}^{-3}$) and carrier mobility ($224 \text{ cm}^2 \text{ V}^{-1} \text{ s}^{-1}$) in the Sb-doped Ge epilayers. The measured MIR reflectivities of the Sb-doped Ge films show free-carrier-dependent properties, which leads to tunable real and imaginary parts of permittivities. Localized surface plasmon polaritons of the bowtie antennas fabricated from the Sb-doped Ge films are demonstrated. The fabricated antennas can provide signal enhancement for the molecular vibrational spectroscopy when these vibrational lines are spectrally in proximity to the localized plasmon resonance. These CMOS-compatible Sb-doped Ge epilayers offer a platform to study the interaction of MIR plasmon with nanostructures on chips.

KEYWORDS: plasmonics, mid-infrared, antimony-doped germanium, high-plasma-frequency, low loss



INTRODUCTION

Plasmonics has the potential to enable unique applications, as it offers a well-designed way to confine electromagnetic waves beyond the diffraction limit with giant field enhancement. For plasmonic building blocks (waveguide, antennas, etc), their constituting materials determine not only the operation wavelength but also the device performance and on-chip integration ability. Plasmonics in noble metals (i.e., Au, Ag)^{1–3} and transparent conductive oxides^{4–6} has already attracted great interests in the visible and the near-infrared for applications in light harvesting^{7,8} and data communications.⁹ In contrast, mid-infrared (MIR) plasmonics show matched resonance with the molecular “fingerprint” absorption spectra,^{10–12} making it appealing for medical diagnostic, environmental monitoring, and security check. Similarly, heavily doped semiconductors^{13–16} (in terms of grown films^{17–20} and chemically synthesized nanostructures^{21–24}) could be the first choice to produce plasmonics in the MIR range, since their plasma frequencies fall well in that region. The doping property of the semiconductors enables tuning of the plasma frequency by changing the free carrier concentration in a wide range (usually between 10^{17} and 10^{20} cm^{-3}). Apart from their eminent plasmonic tunability, heavily doped semiconductors outperform noble metals due to (1) low radiative loss,²⁵ (2) high field confinement in MIR,²⁶ and (3) integration with the existing optoelectronic circuits.

Doped III–V semiconductors are first considered as alternative MIR plasmonic materials owing to their small conductivity effective mass. The doping concentration of the existing III–V plasmonic materials^{27,28} generally falls into the range of 10^{18} to 10^{19} cm^{-3} . For example, Te-doped GaAs with a carrier concentration of $7 \times 10^{18} \text{ cm}^{-3}$ and the corresponding plasma frequency of 795 cm^{-1} has been reported.²⁷ Although there are few reports^{29,30} of doped III–V semiconductors with high doping levels above $\sim 10^{20} \text{ cm}^{-3}$, they are not intended for MIR plasmonics. Using δ -doping technique,²⁹ Si-doped GaAs with a two-dimensional doping concentration of $2 \times 10^{13} \text{ cm}^{-2}$ (corresponding to a three-dimensional doping concentration of $9 \times 10^{19} \text{ cm}^{-3}$) has been obtained; however, homogeneously doped GaAs layer can hardly be obtained with the δ -doping technique. The comparatively low doping concentration of III–V semiconductor can be attributed to the effect of compensation,³¹ in which IV dopant acts as a donor on a group III sublattice site or as an acceptor on a group V sublattice site. The III–V MIR plasmonic materials also present inevitable dipole-active optical phonons, which can complicate the MIR plasmonic behavior^{32,33} and accelerate the recombination process of the photoexcited carriers.³⁴ Fur-

Received: March 11, 2019

Accepted: May 6, 2019

Published: May 6, 2019

thermore, it is worth mentioning that the manufacturing processes of the III–V semiconductors are incompatible with the present Si-CMOS technology.


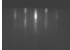

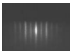
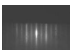

Compared to the III–V compound semiconductors, the CMOS-compatible group IV elemental semiconductors^{35–37} free from dipole-active optical phonons are more desirable for MIR plasmonics. So far, plasma-enhanced chemical vapor deposition-grown (at high substrate temperature above 500 °C) phosphorus (P)-doped Ge epilayer with a doping level of $\sim 10^{19} \text{ cm}^{-3}$ and a plasma frequency of 1160 cm^{-1} has been reported.³⁸ For the dipole antennas based on these P-doped Ge epilayers,³² the signal of the characteristic molecular absorption in the hot spot is found to be 100 times stronger than those deposited on the bare Si substrate due to the huge localized surface plasmon polaritons (SPP) enhancement, opening the possibility for high-sensitivity plasmon-enhanced infrared spectroscopy. Very recently, an activated carrier concentration of $\sim 2.1 \times 10^{20} \text{ cm}^{-3}$ with the corresponding plasma frequency reaching $\sim 3000 \text{ cm}^{-1}$ in the P-doped Ge films is reported.³⁹ Still, the P-doped Ge epilayers suffer from high momentum scattering loss (the intrinsic electron mobility as low as $76 \text{ cm}^2 \text{ V}^{-1} \text{ s}^{-1}$ at a free carrier concentration of $2.1 \times 10^{20} \text{ cm}^{-3}$). In comparison to P-doped Ge epilayers on Si, the Sb-doped Ge films fabricated with molecular beam epitaxy (MBE) method possess two unique features: (1) lower momentum scattering loss (related to the momentum scattering rate Γ and the electron mobility μ of the material), as the electron mobility μ of Sb is higher than that of P^{40,41} ($\mu = 72 \text{ cm}^2 \text{ V}^{-1} \text{ s}^{-1}$ for P⁴² and $\mu = 170 \text{ cm}^2 \text{ V}^{-1} \text{ s}^{-1}$ for Sb at a given doping concentration of $1 \times 10^{20} \text{ cm}^{-3}$; see Figure S1 for detailed comparison) and (2) high doping concentration and high plasma frequency owing to the MBE process combined with moderate substrate temperature (150–350 °C).

This paper focuses on creating excellent plasmonic materials out of Sb heavily doped Ge-on-Si epilayers and investigating their applicability in MIR sensing. With proper choice of dopant species (i.e., Sb) and optimization of growth parameters, the electrical and optical properties are significantly elevated. The excitation of localized SPP in the bowtie antennas fabricated with the Sb-doped Ge-on-Si epilayers is demonstrated. By taking effective loss of localized SPP into considerations, the plasmonic performances of the bowtie antennas with varying carrier concentrations are systematically evaluated. Finally, the fabricated bowtie antennas are used for signal enhancement for the molecular vibrational spectroscopy.

EXPERIMENTAL SECTION


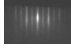

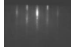
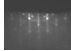

Two series of Sb-doped Ge films are grown on Si substrates with a constant Ge deposition rate of 0.5 \AA/s (see Tables 1 and 2) by molecular beam epitaxy (MBE) system. The base pressure of the MBE chamber is maintained under 2×10^{-10} Torr. The flux monitoring of Sb is performed by a quadrupole mass spectrometer. The substrate temperature is calibrated with a Pt/PtRh thermocouple incorporated in a Si substrate. In the first series (Table 1, A₁–A₆), we investigate the dependence of doping properties on Sb flux at a constant substrate temperature of 250 °C, with the Sb flux varying from 1.0×10^{11} to $2.9 \times 10^{12} \text{ cm}^{-2} \text{ S}^{-1}$; in the second series (Table 2, B₁–B₅), we focus on the dependence of doping properties on substrate temperature at a constant Sb flux of $1.4 \times 10^{12} \text{ cm}^{-2} \text{ S}^{-1}$, with the substrate temperature varying from 150 to 350 °C. When the substrate temperature is as low as 150 °C (sample B₁), crystallinity plays an important role in the electrically active Sb concentration. Therefore, heavily doped Ge films grown on Ge virtual substrate⁴³ (a $1 \mu\text{m}$ thick undoped Ge epilayer between the silicon substrate and the

Table 1. n-Ge Parameters (Plasma Frequency ω_p , Momentum Scattering Rate Γ , Thickness of the Film d , Free Carrier Concentrations n , and Conductivity σ) Dependence on Sb Flux at a Constant Growth Temperature of 250 °C, with Sb Flux Varying from 1.0×10^{11} to $2.9 \times 10^{12} \text{ cm}^{-2} \text{ S}^{-1}$ ^a

Series 1	Sb flux ($\text{cm}^{-2} \text{ S}^{-1}$)	ω_p (cm^{-1})	Γ (S^{-1})	d (μm)	n_{IR} (cm^{-3})	n_{Hall} (cm^{-3})	σ (S m^{-1})	RHEED patterns
A ₁	2.9E12	1979	9.1E13	0.96	8.55E19	9.30E19	2.34×10^5	
A ₂	1.4E12	2086	8.3E13	0.98	9.50E19	1.00E20	2.72×10^5	
A ₃	7.4E11	1327	7.7E13	1.02	3.85E19	3.96E19	1.22×10^5	
A ₄	3.5E11	1024	7.7E13	0.95	2.29E19	2.27E19	6.87×10^4	
A ₅	2.1E11	763	6.2E13	0.98	1.27E19	1.22E19	4.54×10^4	
A ₆	1.0E11	498	5.5E13	0.97	5.42E18	5.01E18	2.07×10^4	

^aThe free carrier density $n_{\text{IR(Hall)}}$ is obtained from the Fourier transform infrared (FTIR) spectrum and the Hall measurement, respectively. Reflection high-energy electron diffraction (RHEED) patterns of Sb-doped Ge films (A₁–A₆) grown directly on Si substrate were shown.

Table 2. n-Ge Parameters (Plasma Frequency ω_p , Momentum Scattering Rate Γ , Thickness of the Film d , Free Carrier Concentrations n , and Conductivity σ) Dependence on Growth Temperature at a Constant Sb flux of $1.4 \times 10^{12} \text{ cm}^{-2} \text{ S}^{-1}$, with Growth Temperature Varying from 150 to 350 °C^a

Series 2	Subs. temp. (°C)	ω_p (cm^{-1})	Γ (S^{-1})	d (μm)	n_{IR} (cm^{-3})	n_{Hall} (cm^{-3})	σ (S m^{-1})	RHEED patterns
B ₁	150	*	*	*	*	1.41E15	*	
B _{1v}	150	2587	6.7E13	0.95	1.46E20	1.47E20	5.38×10^5	
B ₂	200	2430	9.1E13	1.00	1.29E20	1.31E20	3.40×10^5	
B ₃ (A ₂)	250	2086	8.3E13	1.02	9.50E19	1.00E20	2.72×10^5	
B ₄	300	1881	1.0E14	0.98	7.72E19	7.69E19	1.81×10^5	
B ₅	350	598	1.4E14	1.00	7.80E18	7.69E18	1.23×10^4	

^aB₁–B₅ were Sb-doped Ge films grown directly on Si substrate, and B_{1v} was the one grown on Ge virtual substrate.

n-type Ge layer, sample B_{1v}) were also prepared for comparison. Samples B₂–B₅ (with substrate temperature varying from 200 to 350 °C) were still grown on Si substrates, since they can maintain good epitaxial properties as well as high electrically active Sb concentrations without the aid of virtual substrate.

The resulting Sb-doped Ge films are characterized by reflection high-energy electron diffraction (RHEED; RH 20 SS, Stable INSTRUMENTE, Germany) for their detailed crystalline quality and surface smoothness. The Hall measurement (LakeShore 8400

Series) with van der Pauw configuration is performed to retrieve the electrical properties, including conductivity, carrier concentrations, and carrier mobilities. The normal-incidence reflectance spectra $R(\omega)$ are measured with a Fourier transform infrared (FTIR) spectroscopy (Bruker, VERTEX 70). Complex permittivities of Sb-doped Ge films are extracted from $R(\omega)$ by fitting the FTIR data with Drude–Lorentz dispersion model, consisting of one Drude oscillator and two Lorentz oscillators³⁸ (more information about the fitting process is discussed in Section A of the Supporting Information).

$$\varepsilon = \varepsilon' + i\varepsilon'' = \varepsilon_{\infty} \left[1 - \frac{\omega_p^2}{(\omega^2 + i\omega\Gamma)} \right] + \sum_{j=1}^2 \frac{S_j^2}{(\omega_j^2 - \omega^2) - i\omega\Gamma_j} \quad (1)$$

where ε_{∞} is the high-frequency dielectric constant ($\varepsilon_{\infty} \approx 16$ for Ge); $\omega_p = (ne^2/\varepsilon_0\varepsilon_{\infty}m_c)^{1/2}$ is the plasma frequency; $\Gamma = e/\mu m_c$ is the momentum scattering rate;³⁷ and S_j , ω_j , and Γ_j are the strength, resonance frequency, and damping of the Lorentz oscillators, respectively. Parameters related to ω_p and Γ are listed: ε_0 is the permittivity of free space, m_c is the conductivity effective mass ($m_c = 0.12 m_0$ for Ge), n is the carrier concentration, and μ is the carrier mobility.

Furthermore, the bowtie antennas are fabricated out of Sb-doped Ge films by using electron beam lithography and reactive ion etching techniques. Both finite-difference time-domain (FDTD) simulations and optical characterizations (FTIR spectroscopy) are performed to demonstrate localized SPP. The fabricated bowtie antennas are then spin-coated with poly(methylmethacrylate) (PMMA) films, featuring strong vibrational signature at $\omega \sim 1730 \text{ cm}^{-1}$ (carbonyl-bond stretch).

RESULTS AND DISCUSSION

As indicated by RHEED patterns in Tables 1 and 2, sample B₁ is shown to be amorphous due to the relatively lower substrate temperature (150 °C). On the contrary, crystalline defects such as polycrystalline structures appear if the substrate temperature is above 300 °C (B₄, B₅) or the Sb flux exceeds $2.9 \times 10^{12} \text{ cm}^{-2} \text{ S}^{-1}$ (A₁). These defects can lead to significant reduction of free carrier concentrations. However, when Ge virtual substrate is inserted between the Si substrate and the doped Ge layer, the sample (B_{1V}) is observed to be epitaxially grown (the same 150 °C low temperature as that for Ge layer on bare Si substrate (B₁)).

Figure 1 presents the evolution of electric properties of the Sb-doped Ge layers as the growth parameters (i.e., Sb flux and substrate temperature) are varied. In general, the carrier concentration n_{Hall} can be adjusted from 5.0×10^{18} to $1.5 \times 10^{20} \text{ cm}^{-3}$. Specifically, as the Sb flux rises (lower than $1.4 \times 10^{12} \text{ cm}^{-2} \text{ S}^{-1}$), the carrier concentration n_{Hall} and the electrical conductivity σ of A series samples increase correspondingly (Figure 1a). This is due to the Sb atoms, which substitute the sites of Ge lattice in an electrically effective doping process. In addition, excessive Sb flux ($2.9 \times 10^{12} \text{ cm}^{-2} \text{ S}^{-1}$ for sample A₁) can deteriorate the crystallinity and the surface texture of the films (see the RHEED patterns of sample A₁ in Table 1), resulting in the reduction of both the carrier concentration n_{Hall} and the electrical conductivity σ (Figure 1a). Except for the Sb flux, the substrate temperature also influences the electrical properties of the Sb-doped Ge layers. If the substrate temperature is not sufficiently high ($\leq 300 \text{ °C}$), the carrier concentration n_{Hall} and the electrical conductivity σ decrease with the substrate temperature slightly (Figure 1b) due to the segregation on the surface.⁴⁴ The rapid decrease of these two values at high substrate temperature (300–350 °C) is probably due to the existence of polycrystalline defects (see the RHEED patterns of sample B₅ in Table 2).

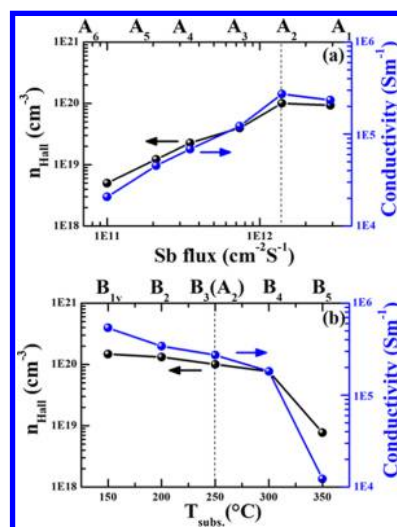


Figure 1. Room-temperature Hall measurements of the Sb-doped Ge layer with (a) varying Sb flux at a constant growth temperature of 250 °C and with (b) varying growth temperature at a constant Sb flux of $1.4 \times 10^{12} \text{ cm}^{-2} \text{ S}^{-1}$.

In Figure 2a,b, we plot the measured reflectivities in the MIR range for the samples (A₁–A₆, B_{1V}–B₅). The reflectivities of all

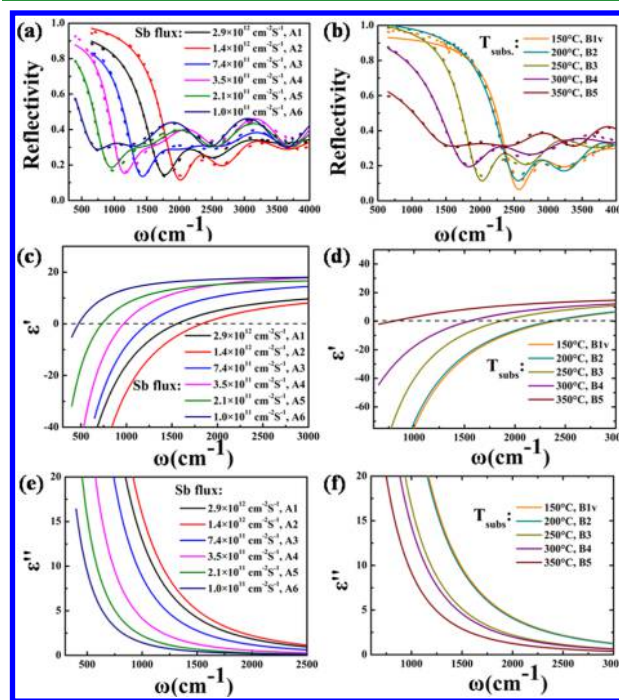


Figure 2. Absolute reflectivity and complex permittivities obtained by fitting the reflectivity data with the Drude–Lorentz formula with (a, c, e) varying Sb flux at a constant growth temperature of 250 °C and with (b, d, f) varying growth temperatures at a constant Sb flux of $1.4 \times 10^{12} \text{ cm}^{-2} \text{ S}^{-1}$. The solid lines are calculated by fitting the experimental data with Drude–Lorentz model.

of the A series and B series samples display a similar sharp decrease as the frequency of incident photons approaches the respective plasma edge (the first dip in the reflectivity). This plasma edge is related to the plasma frequency ω_p , which is continually blue-shifted with the increase of the carrier concentration n_{Hall} . The extracted plasma frequency ω_p in

the MIR range are highly tunable from 498 to 2086 cm^{-1} for the A series and from 598 to 2587 cm^{-1} for the B series. In addition, the extracted real (ϵ') and imaginary (ϵ'') of permittivities in Sb-doped Ge films are shown in Figure 2c–f, respectively. As the carrier concentration n_{Hall} varies, both the real and the imaginary parts of the permittivities for the doped Ge samples show significant deviations. Specifically, as shown in Figure 2c,d, ϵ' becomes more negative as the carrier concentration n_{Hall} increases, indicating an enhanced metallic response. Meanwhile, ϵ'' rises (Figure 2e,f), indicating a larger carrier scattering in the doped Ge films. To verify the reliability of the Hall data, the carrier concentration is also calculated from the IR reflectivity spectrum independently

$$n_{\text{IR}} = \frac{\omega_p^2 m_c \epsilon_0 \epsilon_\infty}{e^2} \quad (2)$$

As shown in Tables 1 and 2, the calculated free carrier concentrations from the reflectivity spectra (n_{IR}) are highly consistent with those obtained from the Hall measurements (n_{Hall}).

Having analyzed the electrical and optical properties of the Sb-doped Ge films, we will examine the localized SPP in the plasmonic structures (i.e., the bowtie antennas made from the doped Ge). The extracted permittivities of the doped Ge material in Figure 2c–f are used in the FDTD electromagnetic simulations. The investigated antenna configuration, shown in Figure 3a, has fixed geometric parameters including apical angle θ (45°), triangular length ($1.4 \mu\text{m}$), gap width ($0.2 \mu\text{m}$), and antenna height ($1 \mu\text{m}$). Electromagnetic field intensity

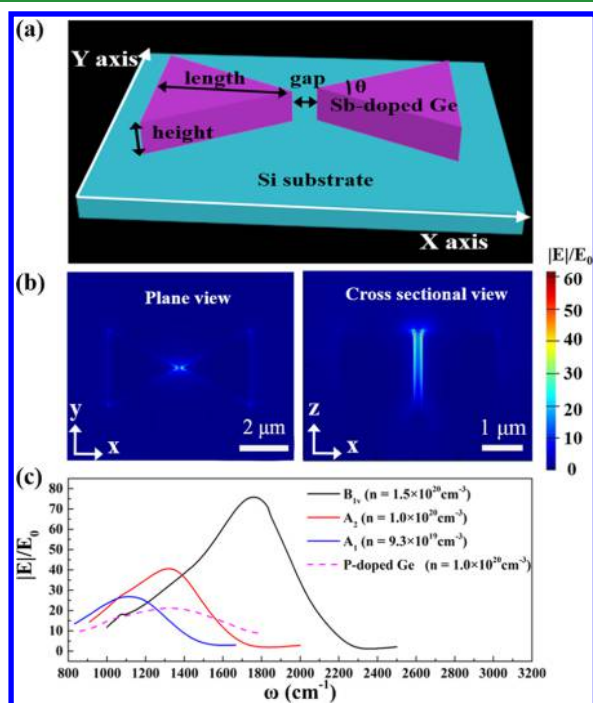


Figure 3. (a) Example of the bowtie antenna with geometric parameters including apical angle θ (45°), triangular length ($1.4 \mu\text{m}$), gap width ($0.2 \mu\text{m}$), and antenna height ($1 \mu\text{m}$). (b) Cross-sectional resonant maps for Sb-doped Ge bowtie antennas with P polarizations ($E||X$ axis). (c) Local field spectra for the Sb-doped Ge platform with varied carrier concentrations (solid line). Field enhancement for P-doped Ge ($n = 1.0 \times 10^{20} \text{cm}^{-3}$) is also drawn for comparison (dashed line).

maps in the plain/cross-sectional view of doped Ge bowtie antennas for P polarization ($E||X$ axis) have been shown in Figure 3b. The field hot spots related to the resonances are located at the gap of two triangular arms. Furthermore, the simulations prove the existence of two plasmonic modes at the bowtie antenna gaps (shown in Figure S2 in Section C of the Supporting Information). The first (air-like) mode lies in the high-frequency range with the field hotspot located at the doped Ge/air interface, while the second (substrate-like) mode lies in the low-frequency range with the field hotspot located at the doped Ge/Si interface.

Afterward, the “air-like” plasmonic mode at the gap is mainly studied. We plot the local field spectra at varying doping concentrations for Sb-doped Ge (also for P-doped Ge with $n = 1.0 \times 10^{20} \text{cm}^{-3}$) in Figure 3c. The devices fabricated with the doped Ge films resonate at their own SPP frequencies and differ greatly in terms of peak field and spectra line shape of the resonances. Specifically, for the Sb-doped Ge samples (B_{1v} , A_2 , A_1), the maximum field enhancement factor $|E|/E_0$ increases monotonically with carrier concentrations, reaching the peak $|E|/E_0$ value of ~ 76 for the highest carrier concentration of $\sim 1.5 \times 10^{20} \text{cm}^{-3}$, with the corresponding plasma frequency of 2587 cm^{-1} (sample B_{1v}). Meanwhile, at the same carrier concentration ($\sim 1.0 \times 10^{20} \text{cm}^{-3}$), higher quality factor of SPP resonance in Sb-doped Ge (sample A_2) is observed than that in P-doped Ge. This echoes with the effective loss theory first proposed to compare metals and alternative plasmonic materials.⁴⁵ More information about the scaling of the effective SPP loss is shown in Section D of the Supporting Information. Figure S3 shows the calculated effective loss rate Γ_{eff} for a plasmonic structure (with a characteristic dimension of $1 \mu\text{m}$) made from Sb-doped Ge with varied concentrations (also for P-doped Ge with $n = 1.0 \times 10^{20} \text{cm}^{-3}$). The doped Ge samples with higher carrier concentrations and mobilities have lower effective loss. Obviously, as the effective loss rate Γ_{eff} is decreased, the higher field enhancement $|E|/E_0$ with narrower quality factor at the resonance for the localized SPP can be envisioned.

We have also fabricated bowtie antenna arrays out of the Sb-doped Ge (sample B_{1v}) with the highest carrier concentration ($n = 1.5 \times 10^{20} \text{cm}^{-3}$) and mobility ($\mu = 224 \text{cm}^2 \text{V}^{-1} \text{s}^{-1}$). Representative scanning electron microscopy (SEM) images of the fabricated bowtie antenna are shown in Figure 4a,b. The triangular length is $\sim 1.8 \mu\text{m}$, the width of the gap between the two triangular arms is $\sim 300 \text{nm}$, and the antenna height is $\sim 1 \mu\text{m}$, while the array period is set to be large enough to prevent the electromagnetic field between the neighboring antennas from overlapping. These geometric parameters are chosen to tune the resonances of the antennas to the desired spectrum positions. As shown in Figure 4c, reflections (R_{ant}) and transmission (T_{ant}) spectra are measured at normal incidence with P polarization ($E||X$ axis) for the bare bowtie antennas. To find the resonances of the antennas, absorption ($A = 1 - R_{\text{ant}} - T_{\text{ant}}$) and normalized extinction spectra ($E_{\text{norm}} = 1 - R_{\text{ant}}/R_{\text{subs}}$) are shown in Figure 4d, with R_{ant} and R_{subs} being the reflection spectra acquired from the antennas and from the substrate, respectively. As predicted by the FDTD simulations in Figure S2, both the absorption and the normalized extinction spectra for the antennas display two resonances, corresponding to two plasmonic modes (i.e., air-like mode: $\sim 1800 \text{cm}^{-1}$; “substrate-like” mode: $\sim 700 \text{cm}^{-1}$).

Plasmonic antennas have been employed as a means to enhance the detection sensitivity of the infrared spectroscopy

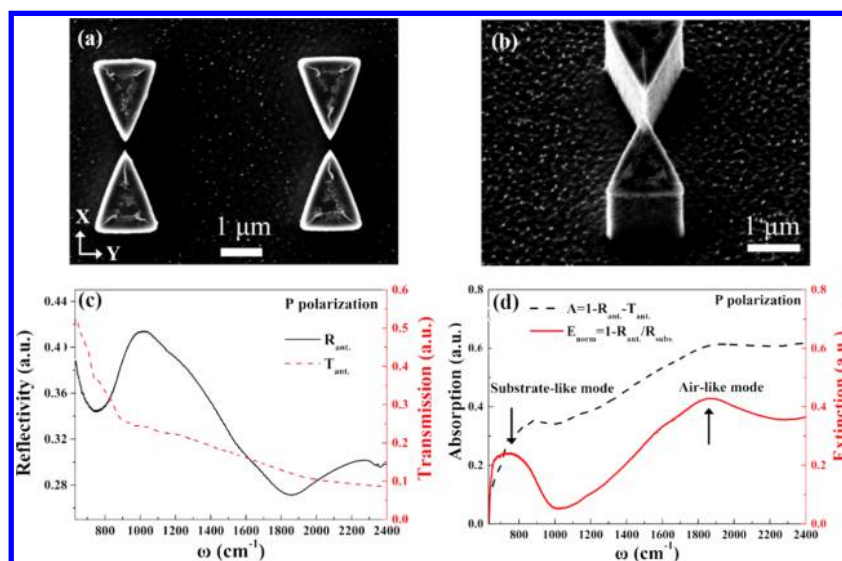


Figure 4. Scanning electron microscopy (SEM) images of the bowtie antennas fabricated out of the Sb-doped Ge (sample B_{1v}) (a) in plain view and (b) from a 45° tilted angle. The geometric parameters include apical angle θ (45°), triangular length (1.8 μm), gap width (0.3 μm) and antenna height (1 μm). (c) Reflection and transmission and (d) absorption and extinction spectra for the bare doped Ge bowtie antennas with P polarizations ($E||X$ axis). These spectra display two resonances, corresponding to two distinct plasmonic modes (i.e., substrate-like and air-like modes).

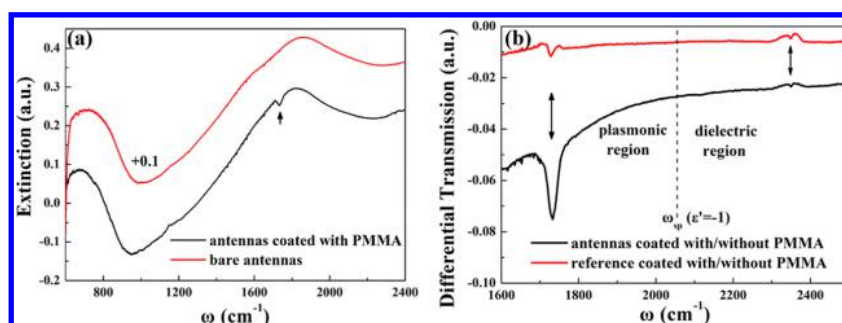


Figure 5. (a) Extinction spectra for bare bowtie antennas (red curve) and bowtie antennas coated with PMMA (black curve). (b) Differential transmission spectra for bowtie antennas (black curve) and for substrate (reference; red curve) with/without PMMA coating. Black arrows indicate fingerprints in PMMA.

in applications of molecular sensing. As shown in Figure 5a, compared to that for the bare bowtie antennas (red line), a red shift of the two plasmonic modes in the normalized extinction spectra (black line) is observed for the PMMA-coated antennas due to the increased dielectric constant in the antenna surroundings. In addition, a strong vibrational fingerprint around $\sim 1730\text{ cm}^{-1}$ (black arrow; carbonyl-bond stretch optical phonon³⁶) appears spectrally in proximity to the air-like mode after the PMMA spin-coating process. Such Fano-like line shapes in the spectra have been extensively studied in the literatures.^{25,39} A minimal detuning in the resonance between the vibrational fingerprint and the plasmonic mode is required for obtaining the maximum molecular signal enhancement in the extinction spectra. We then focus on the extraction of signal enhancement of the vibrational lines. In Figure 5b, differential transmission spectra (transmission spectra difference between samples with/without PMMA coating) for the bowtie antennas (black curve) and for the plain substrate (reference; red curve) display two vibrational lines of PMMA. A strong vibrational signature appears at 1730 cm^{-1} in the range of the plasmonic behavior (below the plasma frequency), while a second fingerprint of a relatively weak vibrational strength appears around 2330 cm^{-1} ,

in the range of the dielectric behavior of the Ge (above the plasma frequency). The relative spectral weight of the signature at 1730 cm^{-1} in the Ge antennas (plasmon-enhanced platform; black line) is much stronger than that in the plain Si substrate (reference; red line), while no signal enhancement is observed for the second fingerprint at 2330 cm^{-1} compared to the reference. These results clearly demonstrate that the signal enhancement originates from the plasmon–phonon coupling²⁵ below the plasma frequency of our material.

CONCLUSIONS

In summary, we have demonstrated the Sb-doped Ge-on-Si epitaxial films as a CMOS-compatible, low-loss, and high-plasma-frequency plasmonic material. The insertion of the Ge virtual substrate between the doped layers and the Si wafers, which also improves the crystalline quality of the doped layers, leads to a high carrier mobility of $224\text{ cm}^2\text{ V}^{-1}\text{ s}^{-1}$ in Sb-doped Ge. By optimizing the growth parameters (i.e., the substrate temperature and the Sb flux), we have succeeded in growing Ge epilayers doped with Sb in 5.0×10^{18} to $1.5 \times 10^{20}\text{ cm}^{-3}$ concentration range, which corresponds to the plasma frequencies in the $498\text{--}2587\text{ cm}^{-1}$ range. We further fabricate the bowtie antennas out of the Sb-doped Ge epilayers and

demonstrate localized SPP with electromagnetic field enhancement in the antenna hot spots and the plasmonic resonance observed in the extinction spectra. The field enhancement at the antenna resonance can be attributed to the inherently high carrier concentration and mobility in Sb-doped Ge, which yield significant reduced effective loss in plasmonic structures. Plasmon-enhanced sensing experiments indicate that the bowtie antennas made from Sb-doped Ge epilayers have the potential to enhance the detection sensitivities for the molecular vibrational spectroscopy when these vibrational lines are spectrally in proximity to the localized plasmon resonance.

■ ASSOCIATED CONTENT

● Supporting Information

The Supporting Information is available free of charge on the ACS Publications website at DOI: 10.1021/acsami.9b04391.

Complex permittivity acquisition with Drude–Lorentz model; scaling of the effective loss; and FDTD simulations of n-type Ge bowtie antenna (PDF)

■ AUTHOR INFORMATION

Corresponding Authors

*E-mail: qiangli@zju.edu.cn (Q.L.).

*E-mail: huiye@zju.edu.cn (H.Y.).

ORCID

Hui Ye: 0000-0003-1084-5376

Author Contributions

H.Y. supervised the project together with Q.L. H.C. conceived the idea, performed the doped Ge deposition, and characterized the sample. Z.X., Z.W., T.B. and M.D. assisted part of the characterization. J.Y. performed the simulations. H.C., H.Y., Q.L., and L.W. wrote the manuscript. All authors discussed the results and contributed to the final version of the manuscript.

Notes

The authors declare no competing financial interest.

■ ACKNOWLEDGMENTS

This research was supported by the National Key Research and Development Program of China (No. 2017YFE0100200), the National Natural Science Foundation of China (No. 61575176), the National Basic Research Program of China (973 Program No. 2013CB632104) and the Research Foundation of State Key Laboratory of Modern Optical Instrumentation (MOI20170001).

■ REFERENCES

- (1) Maier, S. A.; Kik, P. G.; Atwater, H. A.; Meltzer, S.; Harel, E.; Koel, B. E.; Requicha, A. A. Local Detection of Electromagnetic Energy Transport below the Diffraction Limit in Metal Nanoparticle Plasmon Waveguides. *Nat. Mater.* **2003**, *2*, 229.
- (2) Aydin, K.; Ferry, V. E.; Briggs, R. M.; Atwater, H. A. Broadband Polarization-Independent Resonant Light Absorption using Ultrathin Plasmonic Super Absorbers. *Nat. Commun.* **2011**, *2*, No. 517.
- (3) Huang, X. Q.; Tang, S.; Mu, X.; Dai, Y.; Chen, G.; Zhou, Z.; Ruan, F.; Yang, Z.; Zheng, N. Freestanding Palladium Nanosheets with Plasmonic and Catalytic Properties. *Nat. Nanotechnol.* **2011**, *6*, 28.
- (4) Calzolari, A.; Ruini, A.; Catellani, A. Transparent Conductive Oxides as Near-IR Plasmonic Materials: The Case of Al-Doped ZnO Derivatives. *ACS Photonics* **2014**, *1*, 703–709.

- (5) Clavero, C. Plasmon-Induced Hot-Electron Generation at Nanoparticle/Metal-Oxide Interfaces for Photovoltaic and Photocatalytic Devices. *Nat. Photonics* **2014**, *8*, 95.
- (6) Dominici, L.; Michelotti, F.; Brown, T. M.; Reale, A.; Di Carlo, A. Plasmon Polaritons in the Near Infrared on Fluorine Doped Tin Oxide Films. *Opt. Express* **2009**, *17*, 10155–10167.
- (7) Linic, S.; Christopher, P.; Ingram, D. B. Plasmonic-Metal Nanostructures for Efficient Conversion of Solar to Chemical Energy. *Nat. Mater.* **2011**, *10*, 911.
- (8) Ferry, V. E.; Munday, J. N.; Atwater, H. A. Design Considerations for Plasmonic Photovoltaics. *Adv. Mater.* **2010**, *22*, 4794–4808.
- (9) Haffner, C.; Heni, W.; Fedoryshyn, Y.; Niegemann, J.; Melikyan, A.; Elder, D. L.; Baeuerle, B.; Salamin, Y.; Josten, A.; Koch, U.; et al. All-Plasmonic Mach–Zehnder Modulator Enabling Optical High-Speed Communication at the Microscale. *Nat. Photonics* **2015**, *9*, 525.
- (10) Stanley, R. Plasmonics in the Mid-Infrared. *Nat. Photonics* **2012**, *6*, 409.
- (11) Law, S.; Yu, L.; Rosenberg, A.; Wasserman, D. All-Semiconductor Plasmonic Nanoantennas for Infrared Sensing. *Nano Lett.* **2013**, *13*, 4569–4574.
- (12) Mizaikoff, B. Waveguide-Enhanced Mid-Infrared Chem/Bio Sensors. *Chem. Soc. Rev.* **2013**, *42*, 8683–8699.
- (13) Law, S.; Adams, D.; Taylor, A.; Wasserman, D. Mid-Infrared Designer Metals. *Opt. Express* **2012**, *20*, 12155–12165.
- (14) Naik, G. V.; Shalae, V. M.; Boltasseva, A. Alternative Plasmonic Materials: beyond Gold and Silver. *Adv. Mater.* **2013**, *25*, 3264–3294.
- (15) Boltasseva, A.; Atwater, H. A. Low-Loss Plasmonic Metamaterials. *Science* **2011**, *331*, 290–291.
- (16) Soref, R. Mid-Infrared Photonics in Silicon and Germanium. *Nat. Photonics* **2010**, *4*, 495.
- (17) Li, D.; Ning, C. All-Semiconductor Active Plasmonic System in Mid-Infrared Wavelengths. *Opt. Express* **2011**, *19*, 14594–14603.
- (18) Rosenberg, A.; Surya, J.; Liu, R.; Streier, W.; Law, S.; Leslie, L. S.; Bhargava, R.; Wasserman, D. Flat Mid-Infrared Composite Plasmonic Materials using Lateral Doping-Patterned Semiconductors. *J. Opt.* **2014**, *16*, No. 094012.
- (19) Jun, Y. C.; Reno, J.; Ribaudou, T.; Shaner, E.; Greffet, J.-J.; Vassant, S.; Marquier, F.; Sinclair, M.; Brener, I. Epsilon-Near-Zero Strong Coupling in Metamaterial-Semiconductor Hybrid Structures. *Nano Lett.* **2013**, *13*, 5391–5396.
- (20) Panah, M.; Takayama, O.; Morozov, S.; Kudryavtsev, K.; Semenova, E.; Lavrinenko, A. Highly Doped InP as a Low Loss Plasmonic Material for Mid-IR Region. *Opt. Express* **2016**, *24*, 29077–29088.
- (21) Liu, X.; Swihart, M. T. Heavily-Doped Colloidal Semiconductor and Metal Oxide Nanocrystals: an Emerging New Class of Plasmonic Nanomaterials. *Chem. Soc. Rev.* **2014**, *43*, 3908–3920.
- (22) Luther, J. M.; Jain, P. K.; Ewers, T.; Alivisatos, A. P. Localized Surface Plasmon Resonances Arising from Free Carriers in Doped Quantum Dots. *Nat. Mater.* **2011**, *10*, 361.
- (23) Zhou, S.; Pi, X.; Ni, Z.; Ding, Y.; Jiang, Y.; Jin, C.; Delerue, C.; Yang, D.; Nozaki, T. Comparative Study on the Localized Surface Plasmon Resonance of Boron- and Phosphorus-Doped Silicon Nanocrystals. *ACS Nano* **2015**, *9*, 378–386.
- (24) Rowe, D. J.; Jeong, J. S.; Mkhoyan, K. A.; Kortshagen, U. R. Phosphorus-Doped Silicon Nanocrystals Exhibiting Mid-Infrared Localized Surface Plasmon Resonance. *Nano Lett.* **2013**, *13*, 1317–1322.
- (25) Yang, X.; Sun, Z.; Low, T.; Hu, H.; Guo, X.; García de Abajo, F. J.; Avouris, P.; Dai, Q. Nanomaterial-Based Plasmon-Enhanced Infrared Spectroscopy. *Adv. Mater.* **2018**, *30*, No. 1704896.
- (26) Ginn, J. C.; Jarecki, R. L., Jr.; Shaner, E. A.; Davids, P. S. Infrared Plasmons on Heavily-Doped Silicon. *J. Appl. Phys.* **2011**, *110*, No. 043110.
- (27) Chandrasekhar, H.; Ramdas, A. Nonparabolicity of the Conduction Band and the Coupled Plasmon-Phonon Modes in n-GaAs. *Phys. Rev. B* **1980**, *21*, No. 1511.

(28) Iyer, P. P.; Pendharkar, M.; Palmström, C. J.; Schuller, J. A. Ultrawide Thermal Free-Carrier Tuning of Dielectric Antennas Coupled to Epsilon-Near-Zero Substrates. *Nat. Commun.* **2017**, *8*, No. 472.

(29) Schubert, E.; Cunningham, J.; Tsang, W. Electron-Mobility Enhancement and Electron-Concentration Enhancement in δ -Doped n-GaAs at $T = 300$ K. *Solid State Commun.* **1987**, *63*, 591–594.

(30) Zheng, H.; Radhakrishnan, K.; Yoon, S.; Ng, G. Electrical and Optical Properties of Si-Doped InP Grown by Solid Source Molecular Beam Epitaxy Using a Valved Phosphorus Cracker Cell. *J. Appl. Phys.* **2000**, *87*, 7988–7993.

(31) Walukiewicz, W.; Lagowski, J.; Jastrzebski, L.; Rava, P.; Lichtensteiger, M.; Gatos, C.; Gatos, H. Electron Mobility and Free-Carrier Absorption in InP; Determination of the Compensation Ratio. *J. Appl. Phys.* **1980**, *51*, 2659–2668.

(32) Baldassarre, L.; Sakat, E.; Frigerio, J.; Samarelli, A.; Gallacher, K.; Calandrini, E.; Isella, G.; Paul, D. J.; Ortolani, M.; Biagioni, P. Mid-Infrared Plasmon-Enhanced Spectroscopy with Germanium Antennas on Silicon Substrates. *Nano Lett.* **2015**, *15*, 7225–7231.

(33) Nilsson, G. Elements of the IVth Group and IV–IV Compounds. In *Semiconductors: Group IV Elements and III–V Compounds*; Madelung, O., Ed.; Springer: Berlin, 1991; pp 28–42.

(34) Fischer, M. P.; Schmidt, C.; Sakat, E.; Stock, J.; Samarelli, A.; Frigerio, J.; Ortolani, M.; Paul, D. J.; Isella, G.; Leitenstorfer, A.; et al. Optical Activation of Germanium Plasmonic Antennas in the Mid-Infrared. *Phys. Rev. Lett.* **2016**, *117*, No. 047401.

(35) Shahzad, M.; Medhi, G.; Peale, R. E.; Buchwald, W. R.; Cleary, J. W.; Soref, R.; Boreman, G. D.; Edwards, O. Infrared Surface Plasmons on Heavily Doped Silicon. *J. Appl. Phys.* **2011**, *110*, No. 123105.

(36) Calandrini, E.; Venanzi, T.; Appugliese, F.; Badioli, M.; Giliberti, V.; Baldassarre, L.; Biagioni, P.; De Angelis, F.; Klesse, W. M.; Scappucci, G.; Ortolani, M. Mapping the Electromagnetic Field Confinement in the Gap of Germanium Nanoantennas with Plasma Wavelength of 4.5 Micrometers. *Appl. Phys. Lett.* **2016**, *109*, No. 121104.

(37) Soref, R.; Hendrickson, J.; Cleary, J. W. Mid-to Long-Wavelength Infrared Plasmonic-Photonics Using Heavily Doped n-Ge/Ge and n-GeSn/GeSn Heterostructures. *Opt. Express* **2012**, *20*, 3814–3824.

(38) Frigerio, J.; Ballabio, A.; Isella, G.; Sakat, E.; Pellegrini, G.; Biagioni, P.; Bollani, M.; Napolitani, E.; Manganelli, C.; Virgilio, M.; et al. Tunability of the Dielectric Function of Heavily Doped Germanium Thin Films for Mid-Infrared Plasmonics. *Phys. Rev. B* **2016**, *94*, No. 085202.

(39) Pellegrini, G.; Baldassarre, L.; Giliberti, V.; Frigerio, J.; Gallacher, K.; Paul, D. J.; Isella, G.; Ortolani, M.; Biagioni, P. Benchmarking the Use of Heavily Doped Ge for Plasmonics and Sensing in the Mid-Infrared. *ACS Photonics* **2018**, *5*, 3601–3607.

(40) Spitzer, W. G.; Trumbore, F.; Logan, R. Properties of Heavily Doped n-Type Germanium. *J. Appl. Phys.* **1961**, *32*, 1822–1830.

(41) Brotzmann, S.; Bracht, H. Intrinsic and Extrinsic Diffusion of Phosphorus, Arsenic, and Antimony in Germanium. *J. Appl. Phys.* **2008**, *103*, No. 033508.

(42) Mattoni, G.; Klesse, W. M.; Capellini, G.; Simmons, M. Y.; Scappucci, G. Phosphorus Molecules on Ge (001): A Playground for Controlled n-Doping of Germanium at High Densities. *ACS Nano* **2013**, *7*, 11310–11316.

(43) Chong, H.; Wang, Z.; Chen, C.; Xu, Z.; Wu, K.; Wu, L.; Xu, B.; Ye, H. Optimization of Hetero-Epitaxial Growth for the Threading Dislocation Density Reduction of Germanium Epilayers. *J. Cryst. Growth* **2018**, *488*, 8–15.

(44) Oehme, M.; Werner, J.; Kasper, E. Molecular Beam Epitaxy of Highly Antimony Doped Germanium on Silicon. *J. Cryst. Growth* **2008**, *310*, 4531–4534.

(45) Hsieh, W. T.; Wu, P. C.; Khurgin, J. B.; Tsai, D. P.; Liu, N.; Sun, G. Comparative Analysis of Metals and Alternative Infrared Plasmonic Materials. *ACS Photonics* **2018**, *5*, 2541–2548.